Heating Diagnostics with MHD Waves

Y. Taroyan · R. Erdélyi

Abstract The heating of the solar atmosphere is a fundamental problem of modern solar and astrophysics. A review of the seismological aspects of magnetohydrodynamic (MHD) waves with an emphasis on standing longitudinal waves in the context of coronal heating is presented. Efforts made recently may be split into two categories: forward modelling and data inversion. Forward modelling can be applied to predict the observational footprints of various heating scenarios. A new diagnostic method based on the analysis of Doppler shift time series is outlined with specific application to solar coronal conditions. The power of the method is demonstrated and tested using synthetic data and comparing them with actual high-resolution (e.g. SoHO/SUMER) observations. Further, related recent examples of standing longitudinal oscillations in coronal loop structures observed with the new Hinode/EIS instrument are also presented. These latter observations provide an advanced ground for MHD seismology as a tool for plasma heating diagnostics in the atmosphere of the Sun.

Keywords MHD waves · Coronal heating · Forward modelling

1 Introduction

The problem of coronal heating has been challenging solar physicists for the past sixty years. Heating the solar plasma is a fundamental problem in solar physics, astrophysics and space weather forecast, which may also have industrial applications in laboratory devices. Soon after the discovery of the approximately few MK hot plasma in the solar corona theoreticians came up with various physical models trying to explain the apparently controversial behaviour of the temperature in the atmosphere. The key point is the observed distribution

Y. Taroyan (✉) · R. Erdélyi
Solar Physics & Space Plasma Research Centre (SP²RC), Department of Applied Mathematics,
University of Sheffield, Sheffield S3 7RH, UK
e-mail: y.taroyan@sheffield.ac.uk

R. Erdélyi
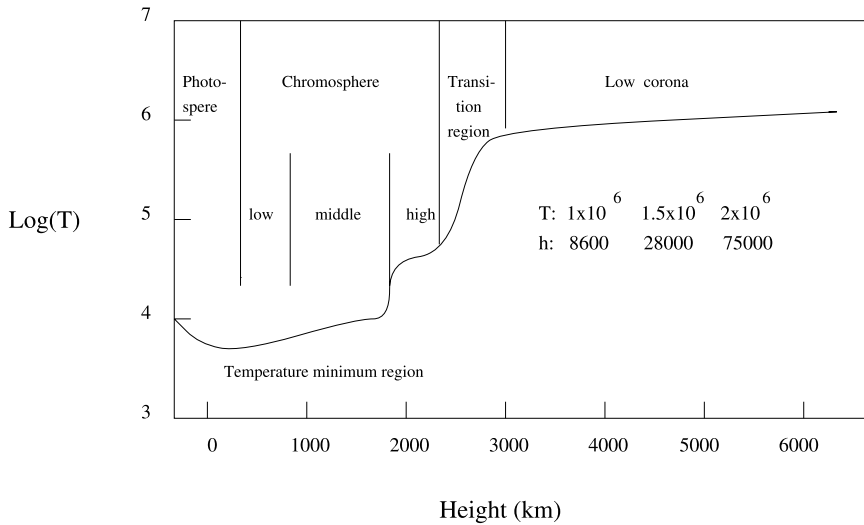e-mail: robertus@sheffield.ac.uk

Fig. 1 The variation of the temperature (on logarithmic scale) in the solar atmosphere as a function of the height measured in km

Table 1 Average coronal energy losses (in $10^4\ \mathrm{erg\,cm^{-2}\,sec^{-1}}$)

Loss by	Quiet Sun	Active region	Coronal hole
Conduction	20	10–10^3	6
Radiation	10	500	1
Solar wind	<5	$<\times 10$	70
Total flux	30	10^3	80

of temperature: solar energy is produced by thermonuclear fusion in the very hot (approximately 14 MK) internal core of the Sun. This vast amount of energy then propagates outwards, initially in the form of radiation (radiation zone) up to a distance of about 0.72 $R_\odot$ and later by convection (in the convective zone) right to the solar surface (photosphere) continuously cooling the solar plasma. Surprisingly, after reaching its minimum at the top of the photosphere (approximately 4200 K), the temperature starts to rise slowly throughout the entire chromosphere (up to around 20,000 K), followed by a very steep and sharp increase in the narrow transition region (few 100,000 K) above 1 MK in the corona (Fig. 1). Maintaining this high temperature requires some sort of input of energy because, without an additional heating the entire corona would cool down by thermodynamic relaxation on a minute-scale. Surprisingly, this non-thermal energy excess to sustain the solar corona is just a reasonably small fraction of the total solar output (see Table 1). It is relatively straightforward to estimate the entire energy budget needed for the solar corona: approximately just a mere 10^{-4} fraction of the Sun's total energy output is needed giving, at least in theory, a fairly easy task for theoreticians to put forward various mechanisms that could divert 0.01% of the total solar output into heating the corona. Numerous theories have been proposed but none has yet been confirmed. Some of the theories rely on sophisticated models, others merely represent concepts or ideas. The task facing a modern-day physicist is to establish *which* of these theories (if any) represents the actual heating mechanism. It is also likely that a combination of heating theories operates in the solar atmosphere (Cargill 1993;

Zirker 1993). Therefore, it is becoming increasingly important to study the *signatures and footprints* of various heating models or to advance even further and make direct comparisons with currently available observational results. Such a forward modelling approach is based on advanced numerical modelling. It narrows down the search for the actual heating mechanism by validating or refuting theoretical models depending on whether or not it is possible to reproduce observations from these models.

In general, any heating process is usually split into three phases: (i) the generation of a carrier of energy; (ii) the transport of energy from the loci of generation into solar atmospheric structures; (iii) and finally the actual dissipation of this energy in the various magnetic or non-magnetic structures of the atmosphere. The operating heating mechanisms in the solar atmosphere can be classified whether they involve magnetism or not. For magnetic-free regions (e.g. in the low chromosphere of quiet Sun) one may suggest a heating mechanisms that can be described within the framework of hydrodynamics (HD). Such heating theories can be classified as hydrodynamic heating. Examples of HD heating are, among others, e.g. acoustic waves and pulsations. However, if the plasma is embedded in magnetic fields, as it is in most parts of the solar atmosphere, the framework of MHD may be the more appropriate approach. These coronal heating theories are called MHD heating mechanisms (for reviews see, e.g., Gómez 1990; Hollweg 1991; Browning 1991; Narain and Ulmschneider 1996; Ulmschneider 1998; Priest and Forbes 2000; Roberts and Nakariakov 2003; Walsh and Ireland 2003; Erdélyi 2004; Klimchuk 2006; Erdélyi and Ballai 2007).

Determining the actual physical behaviour of the coronal plasma from observables is important for understanding the heating mechanism. The observables are obtained using imagers such as the Solar X-ray Telescope (Yohkoh/SXT), the EUV Imaging Telescope onboard the *Solar Heliospheric Observatory* (*SoHO*/EIT), the *Transition Region and Coronal Explorer* (*TRACE*), the Solar Optical Telescope (SOT), X-ray Telescope (XRT) and EUV Imaging Spectrometer (EIS) onboard *Hinode*, *STEREO*, as well spectrometers such as the Coronal Diagnostics Spectrometer (SoHO/CDS), the Solar Ultraviolet Measurements of Emitted Radiation (SUMER), *Hinode*/EIS and others. Currently available instruments still have limited spatial, temporal and spectral resolution in spite of the advanced technologies used when constructing them. Further, inverting the observables is not just an instrumental problem. It is a major theoretical challenge. In this respect, the emerging field of magneto-seismology has great potentials which have not yet been fully exploited. Applications include diagnostics of a range of solar structures from the photosphere to the corona. In solar-terrestrial physics, the term 'seismology' has been traditionally linked with the solar interior. The task of global and local helioseismology is probing the invisible interior of the Sun by measuring the intensity fluctuations or Doppler shifting of the light emitted at the solar surface. Helioseismic inversion has been extremely successful in uncovering the physics of the solar interior. The field of seismology of the solar magnetic atmosphere from the photosphere to the corona is still making first steps. A major obstacle is the difficulty with which the waves and oscillations are detected: firstly, most of the waves are transient and localized in nature. Other inhibiting factors include nonlinearity and strong damping. Unlike in helioseismology where numerous eigenoscillations are detected in a single resonator, usually only one mode is detected in atmospheric structures. It must be stressed here that the study of waves, as possible candidates playing a key role in plasma heating through resonant absorption, phase mixing, ion-cyclotron resonance, non-linear conversion of Alfvén waves, etc., is important in its own right.

The present article reviews recent advances made in heating diagnostics and forward modelling with MHD waves. Forward modelling and inversion represent two important and

complementary tools for studying the heating problem. Section 2 presents the constraints imposed by most recent observations on theoretical modelling. Aspects of forward modelling and inversion are addressed in Sects. 3 and 4. The excitation and damping of slow-mode standing waves in hot loops and the use of these waves for heating diagnostics is discussed in Sects. 5 and 6. Recent Hinode/EIS observations of MHD waves are presented in Sect. 7. Finally, Sect. 8 discusses the potential of a new diagnostic method based on the analysis of Doppler shift time-series.

2 Observational Constraints on Theoretical Models

Observations since Skylab have shown that the heating of the corona is associated with the magnetic activity of the Sun. Instruments on board *SoHO, TRACE, Hinode*, etc., show the presence of loop-like magnetic structures. These instruments have different spatial resolution and temperature coverage, so the loops are bound to look different. Table 1 shows that active regions account for 80–90% of the total coronal heating energy. Therefore, magnetic loop modelling is important for understanding the heating mechanism.

Models of solar atmospheric heating have to comply with observational facts. In the past few years observations have provided new constraints on theoretical models. In closed structures, e.g. in active regions, temperatures may reach up to $8-20 \times 10^6$ K, while in open magnetic regions like coronal holes maximum temperatures may only be around $1-1.5 \times 10^6$ K. Next, observations also show that temperature, density and magnetic field are highly inhomogeneous. Fine structures (e.g. filaments in loops) may have 3–5 times higher densities than densities in their environment. For an excellent textbook on the coronal structures see, e.g., Golub and Pasachoff (1997) and Aschwanden (2006).

The fluctuating brightness and the associated fluctuating velocities as opposed to the quasi-static nature of the corona is a far-reaching observational constraint what is not yet modelled at a satisfactory level. There is also little known about how the heating depends on magnetic field strength, structure size (length, radius, expansion) and age, and, progress is anticipated in the near future. The importance of magnetic fields also resides in their property to channel energy and magnetic stresses from the solar interior and surface to the higher atmosphere. A possible obstacle when discussing the magnetic heating of the atmosphere resides in the difficulties in measuring the magnetic field in tenuous media such as the solar corona using traditional Zeeman splitting or Hanle effect.

A large majority of coronal loops observed by TRACE and EIT (T∼1 MK) were found to be overdense to what would be expected for static equilibrium. The discrepancy was reduced but not eliminated if the heating was assumed to be concentrated near the loop footpoints (Aschwanden et al. 1999, 2001; Winebarger et al. 2003). In contrast, hot ($T > 2$ MK) loops observed by Yohkoh were found to be underdense compared to static equilibrium. Parker (1988) suggested that the corona is heated by many small and localized bursts of energy. These small scale events are called nanoflares. The nanoflare theory predicts that the loops consist of many thin strands which are beyond the spatial resolution of current space borne or ground based instruments. These strands are wound and wrapped around each other due to the continuous shuffling of their photospheric footpoints. This leads to magnetic reconnection between neighboring strands. According to Parker (1988) the energy released by each event is about 10^{24} erg, hence the term nanoflare (i.e., the average energy of a single event is around 10^{-9} times smaller compared to the energy released during a typical flare). Observations of energy releases by solar flares indicate a power law for their energy distribution with a slope of about -1.6 (Crosby et al. 1993). However, Hudson (1991) pointed
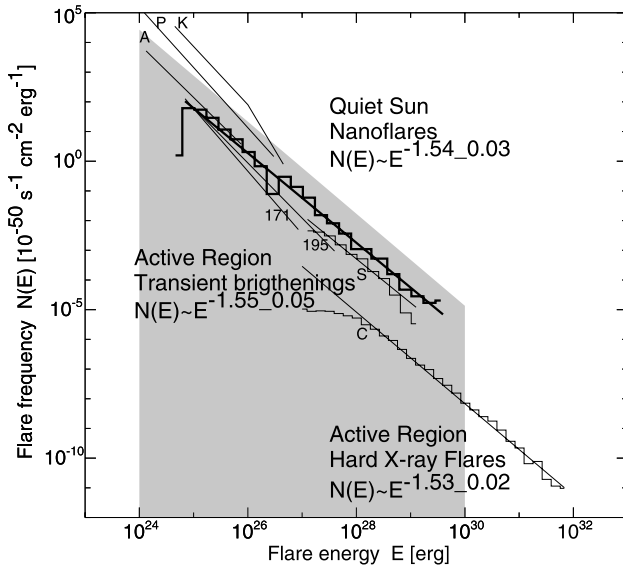
Fig. 2 Compilation of frequency distributions of thermal energies from nanoflare statistics in the quiet Sun, active region transient brightenings, and hard X-ray flares. The labels indicate the following studies: K = Krucker and Benz (1998), Benz and Krucker (2002); P = Parnell and Jupp (2000) (corrected for an erroneous factor of 100 in the original paper); A = Aschwanden et al. (2000); S = Shimizu (1995); C = Crosby et al. (1993), and 171, 195 = Aschwanden and Parnell (2002). The overall slope of the synthesized nanoflare distribution, $N(E) \propto E^{-1.54 \pm 0.03}$, is similar to that of transient brightenings and hard X-ray flares. The *grey area* indicates the coronal heating requirement of $F = 3 \times 10^5 \, \mathrm{erg \, cm^{-2} \, s^{-1}}$ for quiet Sun regions. Note that the observed distribution of nanoflares falls short of the theoretical requirement by a factor of 10 in occurrence rate or a factor of ≈ 3 in energy (from Aschwanden 2006)

out that for the corona to be heated by nanoflares, the slope would need to be more negative than −2, i.e., the nanoflares must satisfy a different distribution function and, therefore, they may be generated by a different physical mechanism. Transient brightenings detected in short loops were statistically studied by Aschwanden and Parnell (2002). The observations were carried out using TRACE for EUV wavelengths and Yohkoh/SXT for soft X-rays. The statistical distribution of the nanoflare/microflare energies was expressed by a power law with an index of around −1.6 or −1.7. Meanwhile Benz and Krucker (2002) found a power index of less than −2. A compilation of frequency distributions of thermal energies from nanoflare statistics is plotted in Fig. 2. There have been other studies as well but no definitive conclusion has been reached yet. A brief summary of power law indices obtained from observations is given by Aschwanden (2006).

Analysis of spectral line profiles shows that optically thin transition region lines display a net red-shift (see, e.g., Chae et al. 1998; Teriaca et al. 1999a; Peter and Judge 1999; Doyle et al. 2002). These red-shifts are often accompanied by blue-shifts at higher temperature lines. The red-shifts have been observed in coronal holes, quiet sun regions, and active regions (see Fig. 3). This observational fact has long been recognized as an important clue to the heating process in the solar atmosphere, prompting several authors to build physical models of a remarkably wide variety to try to account for this phenomenon (see, e.g., Mariska 1987; Spadaro et al. 1990; Hansteen 1993; Sarro et al. 1999; Teriaca et al. 1999b). In addition, Doyle et al. (2002) studied the temporal variability in the Doppler shift of transition region lines. High cadence datasets in C III, O VI and Ne VIII were analyzed in an effort to establish

Fig. 3 Variation of the Doppler shift at disk center with formation temperature of the line. *Error bars* for the data of Brekke et al. (1997) were typically 2 km s^{-1} (not shown). The *solid line* is a by-eye fit to the Doppler shifts from the study by Peter and Judge (1999)
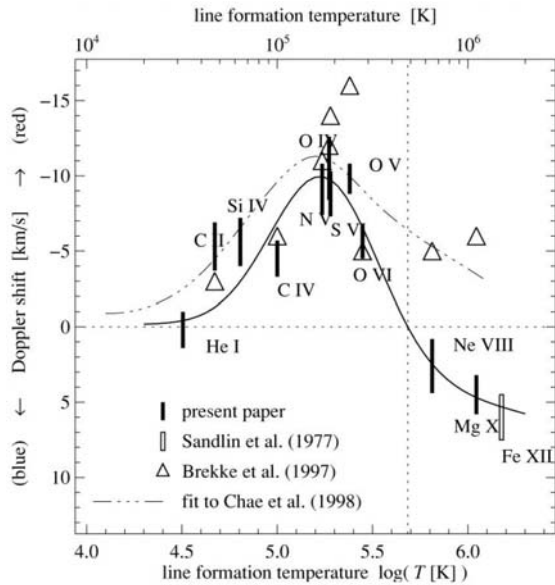
the extent of the Doppler shift variability in different regions of the quiet Sun. Within each of these regions short time-scale variability for the Doppler shift was established. In some cases the line shift could change by 15 km s^{-1} in less than a minute.

The observational constraints on theoretical models are expected to improve since the launch of *Hinode, STEREO, Solar Dynamics Observatory* (*SDO*) and other instruments (e.g., ground-based ROSA). This, in turn, will trigger new advanced forward modelling studies of heating scenarios.

3 Footprints of Heating Mechanisms

The great majority of heating theories assume the presence of both small and large scales. Examples of small scales include resonant layers (Ionson 1978; Poedts et al. 1990; Erdélyi and Goossens 1995, 1996; Sandlin et al. 1977) and current sheets (van Ballegooijen 1986). The large scales are represented by, e.g., coronal loops. This coexistence of multiscales poses a severe challenge for multidimensional numerical modelling since an enormous range of scales must be covered. One possible way of dealing with the problem could be the inclusion of a nonuniform grid whereby grid points are mainly concentrated around small scales. However, many small scale structures become scattered throughout the computational domain as the simulation evolves or could be moved around by flows generated in the system (Ofman and Davila 1996). Another possibility is the use of an adaptive mesh, whereby points are dynamically added or removed. In this case, one has to overcome the problem of the accuracy of the solution at the boundaries between sub-domains with different mesh-size (Keppens et al. 2003). Another way of handling the problem is the use of a multidimensional staggered grid and Lagrangian remap (Arber et al. 2001; Gudiksen and Nordlund 2005a). Currently, many theories rely on one-dimensional modelling to study the plasma response to variations in coronal heating. Simulations of this type, often referred to as loop models, assume that the magnetic field is rigid and plays

only a passive role by channeling the plasma and thermal energy along the field lines. One-dimensional models offer the advantage of highly accurate description of the plasma motion along the field lines. All the important effects are incorporated into the energy equation. The disadvantage is the fact that the heating function cannot be determined self-consistently and must be specified in an artificial way (Klimchuk 2006).

3.1 One-Dimensional Loop Modelling

One-dimensional models are often used to study the signatures and observational footprints of the nanoflares. Patsourakos and Klimchuk (2005) argued that the diagnostics with current instruments such as TRACE and SXT only weakly depend on the spatial distribution of the heating. TRACE is insensitive to the initial hot temperatures. SXT is sensitive to these temperatures, but the densities and emission measures are small until chromospheric evaporation has had time to fill the loop. The emission is therefore mainly detected during the cooling phase of the strands, long after the nanoflare has occurred. Thermal conduction and mass flows are very efficient at redistributing the energies along the strand so the initial differences are rapidly smoothed out. These arguments were supported by the results of one-dimensional modelling.

Similar conclusions were reached by Cargill and Klimchuk (2004) who found that the initial stages of cooling are dominated by thermal conduction and the later stages are dominated by radiative cooling. The loops were found to be underdense at hot SXT temperatures and overdense at cool TRACE temperatures, in agreement with the observations. They also found a broad emission measure distribution with temperatures from 10^5 to 10^7 K.

TRACE observations show uniform emission of material cooling into the passbands. The new XRT instrument onboard the Hinode satellite may have the capacity to register more structured emission along the loop and possibly detect both heating and cooling events due to its broad temperature coverage.

Various aspects of loop heating by random impulses have been studied by Cargill (1994), Walsh et al. (1997), Mendoza-Briceño et al. (2002, 2003, 2005). Taroyan et al. (2006) investigated the evolution of an impulsively heated loop and the spectroscopic consequences of such heating.

The plasma motion along a loop is governed by the following set of nonlinear differential equations:

$$\frac{\partial \rho}{\partial t} + \frac{\partial}{\partial s}[\rho v] = 0,$$

$$\frac{\partial}{\partial t}[\rho v] + \frac{\partial}{\partial s}[\rho v^2] = -\frac{\partial p}{\partial s} + \rho g_{\parallel},$$

$$\frac{\partial e}{\partial t} + \frac{\partial}{\partial s}[(e+p)v] = \rho v g_{\parallel} + \mathcal{H} - \frac{\partial F_c}{\partial s} - \mathcal{L}, \tag{1}$$

where s is the coordinate along the loop, ρ is density, p is pressure, v is velocity,

$$e = \frac{p}{\gamma - 1} + \frac{\rho v^2}{2}. \tag{2}$$

is the energy density, and

$$g_{\parallel} = -g\cos\left(\frac{\pi s}{L}\right) \tag{3}$$

is the component of gravitational acceleration along a semicircular loop of length L. The right-hand side of the energy equation contains sources and sinks of energy. Any type of heating term $\mathcal{H}$ must balance the combined thermal and radiative losses which are the main losses in the corona. Thermal conduction is expressed in terms of the conductive flux F_c:

$$F_c = -\kappa T^{5/2} \frac{\partial T}{\partial s}, \tag{4}$$

with $\kappa = 10^{-6} \, \mathrm{erg \, s^{-1} \, K^{-1} \, cm^{-1}}$ being the coefficient of thermal conduction along the magnetic field. The gradient of conductive flux, i.e., thermal conduction can have both positive and negative values along the loop. It becomes positive in the lower transition region to balance losses due to strong radiation. The last term $\mathcal{L} = n^2 \Lambda(T)$ corresponds to optically thin radiative losses where n is the number density and $\Lambda = \Lambda(T)$ is the radiative loss function. The radiative losses were obtained from a table of values calculated using version 5 of the Chianti atomic database (Dere et al. 1997; Landi et al. 2006), tabulated as a function of temperature and density. Thermal bremsstrahlung is also included in the radiation calculation. The ionization balance is assumed to be in equilibrium and was calculated from the ionization and recombination rates provided by Mazzotta et al. (1998). The element abundances are those due to Feldman (1992).

The chromosphere has an initial depth of 1.5 Mm at each end of the loop and a uniform temperature of $T_{ch} = 20,000$ K. The chromospheric temperature is maintained against radiative losses using the method described by Klimchuk et al. (1987), where the radiative losses are smoothly decreased to zero over a small temperature interval, dT (100 K in the present work), where $T_{ch} \leq T \leq T_{ch} + dT$. This has the effect of maintaining chromospheric stability such that it may act as a source/sink of mass and energy, while avoiding any significant artificial steepening of the radiative loss function at lower temperatures. The boundary conditions are such that the temperature is fixed at 20,000 K and the bulk flow velocity is zero at the edges of the computational domain. The dense chromosphere in the model is sufficient to damp any significant perturbations that may arise, long before they reach the edges of the domain.

Not including the transition region in the model could result in unphysical coronal solutions to the governing equations (1) in the sense that there does not exist a matching solution in the transition region. Further, thermal conduction transfers a large part of the energy deposited in the corona down to the transition region where it is more efficiently radiated due to higher densities and lower temperatures. The transition region is therefore very important for coronal diagnostics and it must be included in the model.

In the following hydrodynamic simulations the heating rate is impulsive, i.e., $\mathcal{H} = \mathcal{H}(t, s)$ depends on both time and distance. The transition region moves up and down in response to changing pressure. Not resolving this region properly could produce significant errors in the coronal quantities. It is clear that an adequate treatment of the hydrodynamic evolution of the loop requires an adaptive mesh. As already mentioned above, points are dynamically added in places where they are needed and removed in places where they are no longer necessary. These features are implemented in HYDRAD (Bradshaw and Mason 2003) which is used to integrate the governing equations (1).

The origin of the energy depositions is unspecified. They could be signatures of nonlinear wave conversion or reconnection. These energy depositions are represented in the form of episodic heating events randomly deposited along the loop at random times. The effects of gravitational stratification, optically thin radiative losses and thermal conduction are all taken into account. The loop is initially kept at a constant chromospheric temperature. The initial stage of the loop evolution is completed about 20 min after the start of the nanoflare
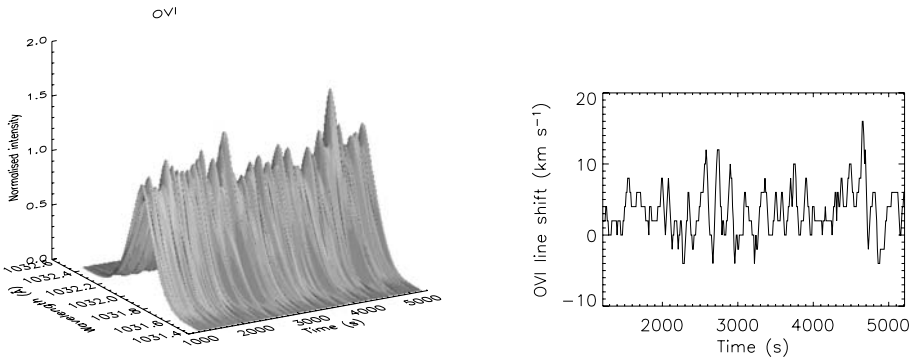
Fig. 4 Evolution of the O VI line profile (*left*) and the corresponding Doppler shift (*right*) in response to an impulsive heating. The net red shift is about 4.2 km s^{-1} (from Taroyan et al. 2006)

heating. During this stage the temperature suffers a gradual increase along the loop and the loop is subsequently maintained at coronal temperatures. A narrow and continuously moving transition region is formed. The displacements could be as large as a Mm. The accuracy of the solution in the transition region is provided by the adaptive mesh. The results are converted into observable quantities by synthesizing the emission line profiles for C IV, O VI, Ne VIII and Mg X. The details of the procedure for the derivation of line profiles are presented in Taroyan et al. (2006). Here we briefly outline the main steps. Positive velocities along the line of sight correspond to red-shift and negative velocities represent blue-shift. The Doppler shift depends on the heliographic position of the loop and the orientation of the loop plane with respect to the slit of the observing instrument. We assume that the observing instrument has typical SUMER characteristics: thus a pixel size of 1″ is taken. The projection of the bulk velocity of the plasma on the line of sight and the corresponding Doppler width are calculated. These are used to calculate the line broadening function and the emissivity of the corresponding line. The emissivity is integrated along a loop segment to obtain the total intensity of the spectral line. The location of the endpoints along the loop is determined by the heliographic position of the loop and its orientation with respect to the observing instrument.

Figure 4 displays the variation of the O VI line profile and the corresponding Doppler shift. The selected resonant lines have peak formation temperatures covering the upper transition region and lower corona. The study reveals that the impulsive nanoflare heating could account for the observed dynamic behavior of the lines. The model also reproduces the average red-shifts seen in the transition region.

3.2 Multidimensional Modelling

Moriyasu et al. (2004) studied the propagation of Alfvén waves generated in the photosphere by random motions. The model included the effects of thermal conduction and radiation. A similar type of model was introduced by Hollweg (1982a, 1982b) and applied to the study of spicule formation and heating (see also Kudoh and Shibata 1999; James and Erdélyi 2002). Moriyasu et al. (2004) found that as the waves propagate upwards they become nonlinear in the chromosphere transition region because of the sharp density decrease and generate slow and fast mode MHD waves and shocks. The plasma is heated at chromospheric heights and the temperature is distributed uniformly along the loop by thermal conduction. The shocks occur one after another leading to episodic heating. Perhaps

Fig. 5 Occurrence frequency of X-ray and EUV "nanoflares" as a function of their peak intensity based on synthetic data (*open circles*: SXT/X-ray; *filled circles*: TRACE/EUV). This shows a power-law distribution with an index −1.7 for SXT/X-ray and −1.9 for TRACE/EUV. Lines are fitted with a power law; *dashed line*: SXT/X-ray; *solid line*: TRACE/EUV (from Moriyasu et al. 2004)
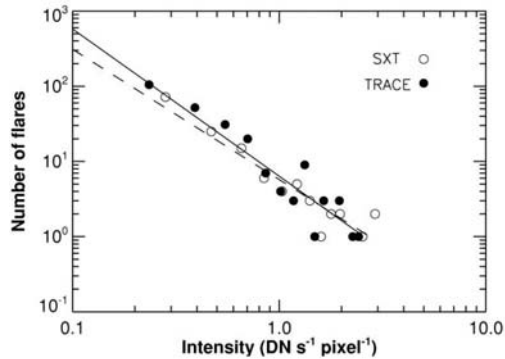
the most important result of this study is that the distribution of the heating events closely matches the power law distribution of the observed transient brightenings (nanoflares) as shown in Fig. 5. It has been mentioned in the Introduction that the occurrence frequency of microflares and nanoflares obeys a power-law distribution with an index close to −2. Thus, the Alfvén wave heating model reproduces the actual observed statistical property of micro/nanoflares rather well. The model therefore suggests the possibility that the observed nanoflares are not reconnection events but MHD shock events generated by Alfvén waves.

Recently Antolin et al. (2008) attempted to find differences in the power law distribution when the loops are heated by Alfvén wave generated MHD shocks and other mechanisms. Van Doorsselaere et al. (2007) showed that any heating mechanism due to the damping of line-tied oscillations should be dominated by a resistive phenomenon in order to accommodate the constraint of footpoint heating. In contrast to this, mechanisms associated with viscous damping lead to apex heating. They found that the analytical and numerical estimates of the heating scale height for the resonant absorption damping mechanism reproduces the observed scale-height. Profiles of heating by MHD turbulence were studied by Buchlin et al. (2007). Alfvén waves are excited by granular motions in the photosphere and propagate upwards into the corona where MHD turbulence sets in and the energy cascades from large scales into small scales. They found uniform heating for loops with constant cross-section and footpoint heating in the case of expanding loops. The most important result of their study is the established strong dependence of the average heating profile on the kinetic and magnetic diffusion coefficients. Different profiles of kinematic viscosity and magnetic diffusivity lead to different heating profiles. The heating is enhanced in places where the dominant transport coefficient is enhanced. Gómez and Dmitruk (2008) have demonstrated that the power law distribution could be a consequence of turbulent heating.

Based on the results of Gudiksen and Nordlund (2005a, 2005b) and Peter et al. (2004), Aschwanden et al. (2007) have argued that observations show no evidence of local heating in the corona. Instead one should be studying possible heating in the upper chromosphere or transition region with subsequent chromospheric evaporation. Aschwanden et al. (2007) presented a number of arguments in support of this idea. A loop that is locally heated in the corona will first brighten up and dim in an EUV filter and subsequently in soft X-ray unless the heating is more rapid than the observing cadence. However, there is little evidence for loop heating being observed in EUV. On the other hand, such behavior could be explained if the heating occurs in the chromosphere/transition region with subsequent chromospheric evaporation.

Other arguments include upflows of hot material and downflows of cool material, the overdensity of coronal loops, upward propagating slow waves, the complexity of the mag-

netic field at low altitudes providing favourable environment for small scale reconnection events such as blinkers, explosive events, transient brightenings, etc., the large loop cross-sections and the current dissipation at transition region heights as evidenced by 3D numerical simulations. The only caveats of the scenario are the non-detection of the initial heating events and the lack of observed upflows.

The above listed results show that the footprints of various heating mechanisms often overlap. Therefore, future forward modelling studies must attempt to disentangle the signatures and footprints of various heating scenarios. The forward modelling approach is anticipated to receive further impetus from the observational constraints provided by the new missions.

4 The Problem of Inversion

Forward modelling is used to derive footprints and observables predicted by various theoretical models. The previous section has shown the difficulties and some of the recent developments in the field. The reverse procedure of deriving the actual footprints and physical quantities from the observations is even harder. Developing reliable inversion methods is not just an observational task. New theoretical ideas can be rather useful in developing novel inversion techniques.

Perhaps the most well known example of the controversy in the field is a single dataset from which three different temperature and heating profiles along a loop were derived by three different authors: uniform (Priest et al. 1998), footpoint (Aschwanden 2001) and apex (Reale 2002) heating. The discrepancy between the results was mainly attributed to the different ways in which the background was subtracted. Other authors have criticized the assumption of isothermal approximation which is implicit in the conventional filter ratio analysis (Landi and Landini 2005; Schmelz and Martens 2006).

As mentioned in the previous section, most studies have shown lack of evidence for loop heating being observed in EUV. Recently Reale and Ciaravella (2006) have applied the well-known TRACE filter ratio analysis to measure temperature evolution along a loop. The analysis was based on the fact that the loop faded out at the end of the image sequence and so the last images were used to derive a background. The filter ratio (temperature) with no background subtraction remained flat along the loop, whereas the background subtracted images showed temperature structuring with both heating and cooling taking place along the loop. If proven to be correct, these results could present the first real evidence for heating being observed in EUV.

The results of spectroscopic measurements are probably as conflicting as those derived from imagers. Ugarte-Urra et al. (2005) measured the electron density along a coronal loop observed by CDS and EIT. Different approaches for background subtraction were applied. The electron density was determined spectroscopically from the intensity ratio of lines of the same ion. A comparison with the results of a 1D hydrodynamic simulation suggests preferentially footpoint heating. However, other possibilities cannot be ruled out due to the large uncertainties resulting from insufficient spatial and spectral resolution of CDS. Flows not seen by CDS could also change the conclusions. These results are in contrast to the results of Schmelz and Martens (2006) who used the same CDS to study a coronal loop on the limb. They found broad differential emission measure (DEM) distributions for a number of pixels both before and after the background subtraction was applied. They also found temperature variation along the loop from the footpoint to the apex in contrast to the results derived from TRACE and EIT. New instruments will provide further insight and perhaps

reconcile the discrepancies which currently exist. The XRT instrument on board the Hinode satellite gives the opportunity to construct thermal maps using five or even more filters.

An alternative approach to the inversion problem is the use of MHD waves: an excellent diagnostic tool, the full potential of which has yet to be explored. Flux tubes expand rapidly in height since the magnetic pressure will push field lines apart due to the strong decreases in density. Magnetic flux tubes emerging from the solar interior rapidly expand in the solar atmosphere at about 1,500 km above the photosphere. These flux tubes are continuously shaken and twisted by photospheric motions (i.e. by both granular motion and coherent global acoustic p-mode oscillations). The flux tubes are excellent waveguides with magnetic and compressional perturbations able to propagate along them for a long spatial extent. The photospheric perturbations propagate in the form of various MHD tube waves (e.g. slow and fast MHD waves; Alfvén waves). The dissipation of MHD waves is manifold: these waves couple with each other, damp due to some physical dissipative processes, interact non-linearly, resonantly interact with the closed waveguide (i.e. coronal loops) or they steepen into nonlinear waves (e.g. solitons or shock waves). MHD waves could be used for a number of diagnostic purposes: measuring the magnetic field strength, the fine structure, the transport coefficients in the solar atmosphere, understanding the processes responsible for their damping and so on (see, e.g., De Moortel et al. 2000; Nakariakov and Ofman 2001; Goossens et al. 2002; Ruderman and Roberts 2002; Díaz et al. 2002; Wang et al. 2002; Zaqarashvili 2003; De Moortel and Hood 2003; Ruderman and Erdélyi 2004; Andries et al. 2005; Ballai et al. 2005; Dymova and Ruderman 2005; De Moortel 2005, 2006; Erdélyi and Carter 2006; Erdélyi and Fedun 2006; Erdélyi and Verth 2007; Verth et al. 2007, 2008; Carter and Erdélyi 2007; O'Shea et al. 2007; Jess et al. 2008; McLaughlin and Ofman 2008; Aschwanden and Terradas 2008). For more details on the observed MHD waves, their damping, etc., see reviews by Nakariakov and Verwichte (2005), Banerjee et al. (2007).

De Moortel and Bradshaw (2008) have shown that observational data from imagers and line-integrated intensities from spectrometers alike are subject to misinterpretation due to the non-linear interactions between the parameters that govern the formation (emissivity, ionization balance) and measurement (instrument response function) of emission lines. Both the damping rate and profile, as well as the phase of the oscillations can change and in some cases it is possible that even the period is modified. This does not, in any way, reflect on the quality of the chosen instrument or emission lines. Forward modelling provides a way to guard against the misinterpretation of observational data by allowing one to synthesize the likely observational characteristics of a particular event and, with a priori knowledge of the event, determine how accurately one may have recovered the underlying physics of the event from the observational data alone.

Detection and characterization of coronal oscillatory phenomena with spectroscopic instruments that simultaneously capture many emission lines is particularly important, since it offers the possibility of refining our understanding of the temperature-dependent behaviour of the oscillations. It may also be possible to make simultaneous observations in density-sensitive pairs of emission lines, further constraining the characteristics of the oscillations.

5 Excitation and Damping of Slow-Mode Standing Waves Observed with SoHO/SUMER

Heating and cooling lead to variable mass flows along the loops. Quantifying the heating function is important for understanding the nature of the heating mechanism. In this respect, standing slow-mode (acoustic) waves detected by Wang et al. (2002) and Kliem et al.
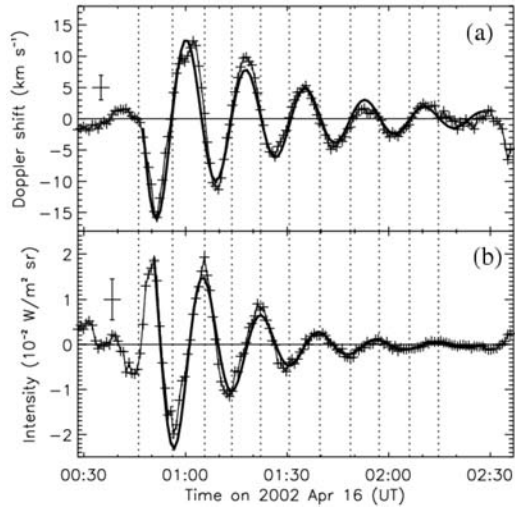
(2002) in hot active region loops could be a useful tool. A large number of Doppler oscillation events were detected by SUMER (Wang et al. 2003a). Although some lines of evidence suggested slow standing waves as the cause of these oscillations, the absence of clear brightness fluctuations with the wave period argued against such an interpretation. Wang et al. (2003b) presented the first example of both intensity and Doppler shift oscillations in a hot ($T > 6$ MK) loop using the SUMER spectrometer. Figure 6 shows the evolution of the intensity and Doppler shift. The physical parameters of the oscillations were measured from the best fit damped sine function. For the Doppler oscillation an amplitude of 18 km s^{-1}, a period of 17 min, and a decay time of 36 min were obtained. The discovery of Doppler and intensity oscillations with the same period and an exact quarter-period phase difference in this study gave for the first time strong evidence in support of slow standing waves. One could argue that a kink-mode motion of the loop may also produce intensity and Doppler oscillations with possibly a quarter-period phase difference when the slit is located at the loop top. However, such an assumption would lead to a plasma β of about 2.4, which would be inconsistent with the usual coronal condition of low β.

The damping of these oscillations was first studied by Ofman and Wang (2002) who concluded that for typical observational solar parameters of the oscillating loops, the dominant wave damping mechanism is thermal conduction, with less significant contribution from compressive viscosity. The left panel of Fig. 7 shows the dependence of the decay time on the period for $T = 6.3$ and 8 MK and the best-fit scaling for both temperatures. The SUMER data for 35 loops are shown for comparison. Ofman and Wang (2002) found that the power of the scaling is 1.17 for the lower temperature and 1.01 for the higher temperature, in agreement with the expected effects on the thermal conduction and viscosity (i.e., increased viscosity and conduction results in higher dissipation rate for the same wave period). The spread in the observational data set was justified by the expected range of temperatures 6 MK $< T <$ 10 MK, loop densities, and wave amplitudes. Mendoza-Briceño et al. (2004) showed that the inclusion of gravitational stratification could reduce the damping time by 10–20% (see the right panel of Fig. 7). The effects of compressive viscosity in stratified loops were examined by Sigalotti et al. (2007). Bradshaw and Erdélyi (2008) found that the radiative emission arising from a non-equilibrium ionization balance will always act to reduce the damping timescale (in comparison to the equilibrium case) and may do so
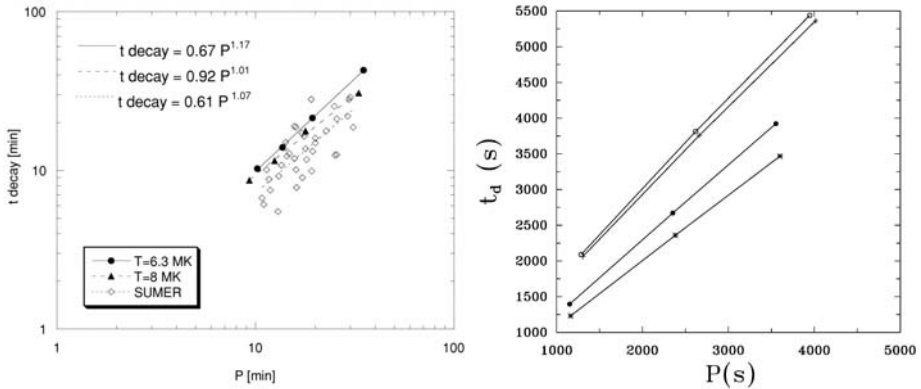
Fig. 7 *Left*: Scaling of the dissipation time of the slow waves with the wave period for and 8 MK. SUMER observations are shown for comparison (from Ofman and Wang 2002). *Right*: Predicted scaling of the decay time with wave period for the stratified and nonstratified loop model calculations with $T = 6.3$ and 8.0 MK. The data set plotted corresponds to models with an initial wave-velocity amplitude of 87 km s^{-1}. The *open circles* give the scaling for $T = 6.3$ MK with no stratification, the *plus signs* for $T = 6.3$ MK with stratification, the *filled circles* for $T = 8$ MK with no stratification, and the *asterisks* for $T = 8$ MK with stratification (Mendoza-Briceño et al. 2004)

by up to 10%. Verwichte et al. (2008) showed that shock dissipation is an important damping mechanism at large amplitudes, enhancing the damping rate by up to 50% above the rate given by thermal conduction alone. Erdélyi et al. (2008) derived a second-order scaling polynomial between the damping time and the parameter determining the apex temperature of a loop.

Results of the numerical simulations by Selwa et al. (2005) showed that initially launched impulses mainly trigger the fundamental mode and its first harmonic, depending on the location of these pulses along a given loop. They found that the standing waves are excited in a dozen or so wave periods and are strongly damped over a similar time-scale. Observations show that these waves are usually preceded by footpoint brightenings. Taroyan et al. (2005) have analytically derived the mathematical form of the heating pulse at the footpoint of a loop which is required to rapidly set up a standing wave. The standing wave is set up in a single period. The main requirement is that the duration of the heating pulse approximately matches the period of the oscillations. The results of the analytical study were confirmed by numerical simulations. Selwa et al. (2007) considered slow standing waves that are impulsively excited in a curved coronal loop. They found that slow waves can be excited faster in curved loops than in slabs due to the combined effect of the pulse inside and outside the loop. Haynes et al. (2008) showed that a kink instability in a short loop initially sets up a second harmonic that is converted through the rearrangement of the magnetic field into two out-of-phase fundamental slow modes. These slow modes are in the two entwined flux tubes created during the kink instability and are subsequently damped by shock dissipation.

6 Heating Diagnostics of hot Loops with MHD Waves

Slow standing modes could be used for a number of purposes: quantifying the heating function (Taroyan et al. 2007a); measuring the magnetic field (Wang et al. 2007); determining the transport coefficients (Ofman and Wang 2002). The present section summarizes results

Fig. 8 The oscillating soft X-ray loop (outlined with *crosses*) fitted with a circular model (*dark curve*). The SUMER spectrometer slit position is indicated as *two vertical lines* (from Taroyan et al. 2007a)
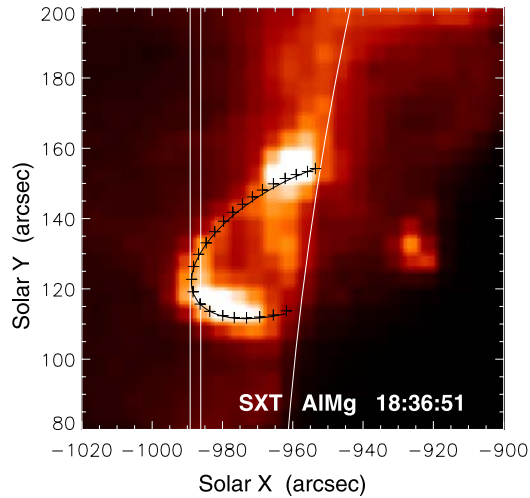
of a case study to demonstrate how a combination of forward modelling and inversion could be used for most efficient diagnostics.

Taroyan et al. (2007a) carried out a combined observational and modelling study of an oscillatory event that occurred on September 17, 2000. Spectral observations of active region corona were obtained by SUMER in sit-and-stare mode. Two neighbouring active regions (AR 9169 and AR 9167) on the north-east limb were observed with a cadence of 90 s using the $4'' \times 300''$ slit during 16–20 September 2000 (Wang et al. 2006, 2007). Five spectral lines, Fe XIX λ 1118 (6.3 MK), Ca XV λ 1098 and λ 555 × 2 (3.5 MK), Ca XIII λ 1134 (2.2 MK), and Si III λ 1113 (0.06 MK) were transmitted, with a 2.2 Å wide window for each line. After processing the raw data following standard procedures (decompression and corrections of flat-field, detector distortions, deadtime, and gain effects), a single Gaussian was fit to each line profile to obtain a Doppler shift time series at each spatial pixel. A large number of flarelike brightenings were revealed in the hot flare line Fe XIX and more than 20% of them are found to be associated with Doppler shift oscillations.

Figure 8 shows a hot coronal loop seen in the SXT AlMgMn filter. The SUMER slit was located on the loop top. Applying a method described by Wang et al. (2003a), it is possible to determine the geometric parameters of the loop based on a circular model. A loop length of 82 Mm is obtained, the azimuth angle of the loop baseline to the east-west direction is 33° and the inclination angle of the loop plane to the vertical is 30°. Assuming that the northern footpoint of the loop is farther than the southern one to the observer, the loop plane should be inclined away from the observer to the vertical in order to match the observed loop shape. With this assumption, the initial blueshifts are expected to behave as observed if the energy release was located near the northern footpoint and produced a plasma injection along the loop. A brightening seen at the northern footpoint indicates a possible microflare (Fig. 8). This brightening appeared at about 18:28 UT. It was accompanied by a flow as suggested by the blue wing enhancement of the Fe XIX line profile. The loop oscillation seems to be set up after 18:35 UT when the line peak position started to move. Therefore, the timing supports the idea that the oscillation could be triggered by a microflare heating at the loop footpoint.

The left panel in Fig. 9 shows evolution of the intensities in Fe XIX , Ca XV (λ 1098) and Ca XIII lines along the SUMER slit observed at the loop top. The brightening first peaked in
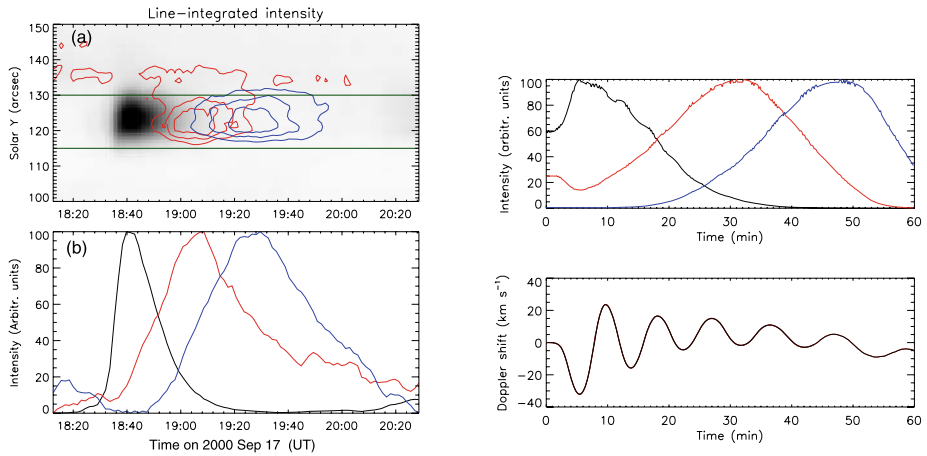
Fig. 9 (Color online) *Left*—SUMER observations: the *top panel* represents the time series of the Fe XIX (*black*) *line* intensity along the slit. The overlaid contours represent the Ca XV (λ 1098, red) and Ca XIII (*blue*) intensity time series. The contour levels are 70, 80, and 90% of the peak intensity; the *bottom panel* is the average time profile of line-integrated intensity along the cut in the *top panel*. *Right*—synthesized observations: the *top panel* shows the simulated time profiles of the line intensities along the slit cut. The *black*, *red* and *blue lines* correspond to Fe XIX , Ca XV (λ 1098), and Ca XIII intensities; the *bottom panel* shows the corresponding Doppler shift (from Taroyan et al. 2007a)

the Fe XIX line at about 18:40 UT, then peaked in the Ca XV and Ca XIII lines about 30 min and 50 min later. This indicates a cooling of the hot loop down to lower temperatures. The cooling was accompanied by a rapidly damped oscillation with a period of about 8 minutes. The maximum initial Doppler shift registered by SUMER was about 30 km s^{-1}. Hydrodynamic simulations were performed using the parameters of the observed loop and including the thermal and radiative losses in the energy equation. The simulation results were converted into observables by applying spectral line synthesis. The comparison between the simulated and observed line profiles was done in three different lines which cover temperatures from 3 to 7 MK. Figure 9 compares the simulated line profiles with the actual SUMER measurements. In both cases, each line suffers an intensity increase followed by a decrease. The initial increase in the Fe XIX line intensity is a consequence of the footpoint brightening seen by Yohkoh/SXT and the corresponding temperature increase. The subsequent decrease represents the cooling phase. The intensities of the cooler Ca XV and Ca XIII lines consecutively pass through their peaks as the loop cools to lower temperatures. The oscillations only appear in the Doppler shift. The initial negative blue shift of about 32 km s^{-1} is followed by a damped oscillation. A successful comparison between the observed and simulated loop behaviour allowed Taroyan et al. (2007a) to

1. establish the nature of the observed oscillations in terms of a fundamental mode standing acoustic wave;
2. confirm that the waves are excited by a microflare occurring at one of the loop footpoints and estimate its energy;
3. determine the evolution of the heating rate along the loop.

Figure 10 displays the inferred time-distance plot for the heating rate (in logarithmic scale). The brightening at the lower footpoint corresponds to the microflare that sets up a standing wave within a single period. The heating rate decreases to 20% of its initial value
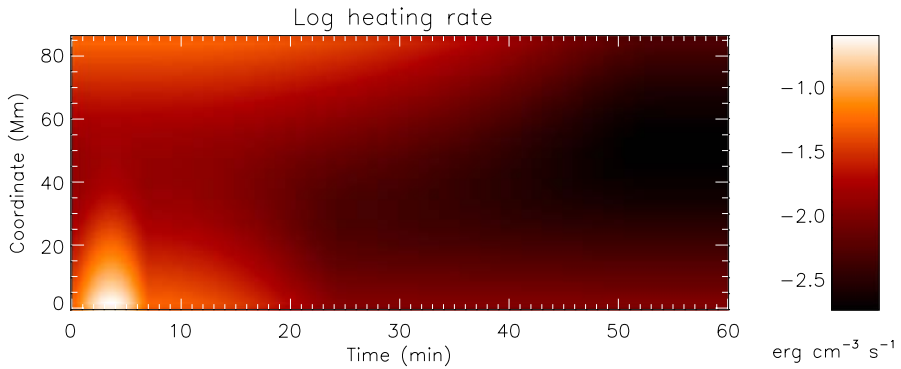
Fig. 10 The heating rate (in logarithmic scale) as a function of time and coordinate along the observed loop. The brightening at the lower footpoint corresponds to the microflare which initiates the fundamental mode standing wave (from Taroyan et al. 2007a)

at the bottom (northern) footpoint in about 25 min. It also decreases to 10% of the initial value at the top (southern) footpoint but on a longer time scale in order to gradually change the net red shift into blue shift as observed.

There is a quarter period phase shift between the velocity and density oscillations. The density oscillation, unlike the velocity oscillation, has a node at the apex and antinodes at the footpoints of the loop. The slit is located around the apex of the loop which explains the absence of intensity oscillations both in the SUMER data and in the simulations. From an observational perspective, the detection of intensity oscillations without accompanying Doppler shift oscillations at the apex could indicate the presence of a second harmonic. The Doppler shift oscillations would be in anti-phase on different sides of the apex. A second harmonic could be excited by a (micro)flare at the apex which would drive flows in opposite directions. Such oscillations have been studied by Nakariakov et al. (2004) in a somewhat different context. The lack of evidence for the presence of the second harmonic in the SUMER data supports the idea that small scale energy releases such as microflares predominantly occur at the footpoints of active region hot loops.

7 Hinode/EIS Observations of Slow-Mode Standing Waves

The EUV imaging-spectrometer Hinode/EIS has two CCDs each covering a 40 Å wavelength range: 170–210 Å and 250–290 Å. The wavelength response of EIS has two peaks at around 195 Å and 271 Å corresponding to the two CCDs. EIS has both narrow ($1''$ and $2''$ wide) slits, and wider ($40''$ and $266''$) imaging slots, all with up to $512''$ in the solar_Y direction. EIS is able to make slit observations of active regions in ten seconds and of the quiet Sun in between thirty and sixty seconds, and of flares in approximately one second. The spectral resolution can be less than $1\,\mathrm{km\,s^{-1}}$ for the Doppler shift. More details of the Hinode/EIS characteristics are given by Culhane et al. (2007) and Kosugi et al. (2007).

Until recently it was not clear why standing longitudinal oscillations were only seen in high temperature lines. Taroyan and Bradshaw (2008) have recently shown that standing waves can be formed in cooler EUV loops in a similar way when all the important effects such as gravitational and thermal stratification, losses, etc., are taken into account. Hot loops are therefore not unique in this respect and there is nothing to prevent the formation of standing waves in cooler loops. Both standing and propagating waves are a natural response of
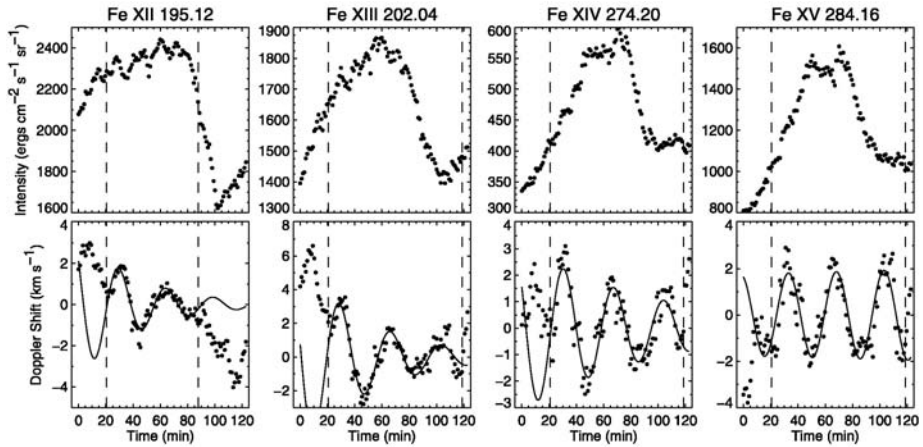
Fig. 11 Averaged intensity and de-trended Doppler-shift data for the emission lines that exhibited Doppler-shift oscillations. The *curves on the lower plots* show the best fit to a decaying sine wave (from Mariska et al. 2008)

the loop plasma to impulsive heating. Simulation results were presented by Taroyan and Bradshaw (2008) in terms of synthetic Hinode/EIS observations to predict the wave footprints in the actual observations. In the case of imaging mode observations with the 40″ slot, the waves are most clearly seen in the EIS Fe XII 195 Å filter when they are just being set up. In contrast, the waves clearly appear in all three lines when spectroscopic observations with the 1″ slit are applied. There is a quarter period phase shift between the intensity and the Doppler shift oscillations indicating the presence of a standing wave. Also, the intensity oscillations suffer phase variations when the plasma undergoes heating or cooling. The case study showed that standing acoustic waves in EUV loops are most likely to be detected using spectroscopic observations.

Mariska et al. (2008) reported the detection of low-amplitude damped oscillations in coronal emission lines formed at EUV temperatures observed with the EUV Imaging Spectrometer on the Hinode satellite. The observations were centered at the southwest limb on January 14, 2007. A sit-and-stare observation began at 12:30:12 UT and consisted of 120 exposures with the 1″ slit, each with an exposure time of 60 s. Each exposure covered nine data windows on the EIS detectors. The oscillations had an amplitude of about 2 km s^{-1} and a period of around 35 minutes. The decay times showed some evidence for a temperature dependence with the emission line of lowest temperature (Fe XII 195.12 Å) exhibiting a decay time of about 43 minutes, while the emission line of highest temperature (Fe XV 284.16 Å) showed no evidence for decay over more than two periods of the oscillation. The authors argued that the observed oscillation is the result of a heating event in a nearby structure that appeared to be magnetically connected to the area where the oscillations were observed. Assuming that a loop was being observed, the oscillations were near one footpoint. The distance between the two footpoints would roughly be 218 Mm. A semicircular loop with this diameter would then have a length of approximately 342 Mm. This is within a factor of 2 of the value expected for a standing magnetoacoustic wave oscillating in the fundamental mode. The locations of the footpoints are highly uncertain, especially since they are very close to the limb, and the loop geometry is difficult to determine. Nevertheless, the data appear to be consistent with slow magnetoacoustic standing waves, but may be inconsistent with conductive damping.
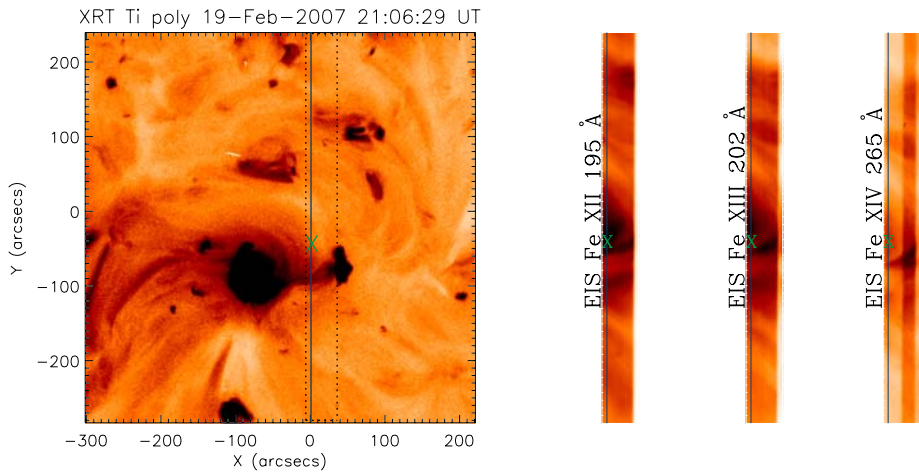
Fig. 12 *Left*—Hinode/XRT image of the solar disc taken 2007 February 19, 2007. The *dotted rectangle* shows the region of interest in which EIS imaging/spectroscopic observations were carried out. The 1″ EIS slit is marked by a *vertical line*. The *cross* indicates the location of the pixels that registered the oscillations starting at 21:06 UT. *Right*—Hinode/EIS 40″ slot observations lasting from 22:10 to 22:35 UT. Each image covers a $40″ \times 512″$ rectangular area that is marked by a *dotted line* in the *left panel* (from Erdélyi and Taroyan 2008)

Erdélyi and Taroyan (2008) have recently presented the first example of standing acoustic waves in cool loops that contain both intensity and Doppler shift oscillations. The 2007, February 19 observations are sit-and-stare observations in which a 1″ wide EIS slit with a window height of 512″ is used. The observations began at 21:06 UT and lasted for about an hour. The location of the slit is marked by a vertical line in the XRT image and in the EIS 40″ slot images taken after 22:10 UT. The exposure time was around 30 seconds and the total number of exposures 110. The centre of the slit has average coordinates solar_X $= 6″$, solar_Y $= -35″$. Standard procedures for EIS data reduction were applied to include calibrating the data and creating error arrays, applying Gaussian fitting to each line profile and correcting for the slit tilt and orbital variation. The resulting intensities and Doppler shifts were measured in DN (data number) and in $km\,s^{-1}$. The Doppler shift has an error of less than $1\,km\,s^{-1}$.

Oscillatory behaviour was detected between pixels 230 and 234. These pixels are marked in the XRT and EIS images (Fig. 12). In order to verify that the oscillations are not an instrumental artifact, the Doppler-shift time series along the entire slit was examined (Fig. 13). Except for the narrow horizontal stripe, no significant wave power was found elsewhere along the slit. An average of the intensity and the Doppler shift taken over these pixels for Fe XIX 195 Å, Fe X 184.7 Å, and Fe XIII 202 Å is plotted in Fig. 14. The oscillations show up both in the intensity and in the Doppler shift, which appear to be phase-shifted by a quarter period as shown by the sinusoidal fit. The maximum amplitude for the Doppler shift is about $4\,km\,s^{-1}$.

Wavelet analysis was applied the details of which are given by Torrence and Compo (1998). A randomization method was implemented to estimate the significance level of the peaks in the wavelet spectrum. The wavelet for the Doppler shift showed strong power at 1.2 mHz for almost the entire duration of the observations. The corresponding power in the global wavelet has a significance level above 99%. A similar wavelet analysis procedure

Fig. 13 (Color online)
Doppler-shift time series along
the 1″ EIS slit for the
observations starting at 21:06 UT
on 2007 February 19. Positive
and negative Doppler shifts are
represented by *red* and *blue
colours*, respectively. The
selected line is Fe XIX 195 Å.
The exposure time is 30 seconds
and the total number of exposures
110. The narrow stripe between
the *horizontal dashed lines* marks
the pixels with high oscillation
power and corresponds to the
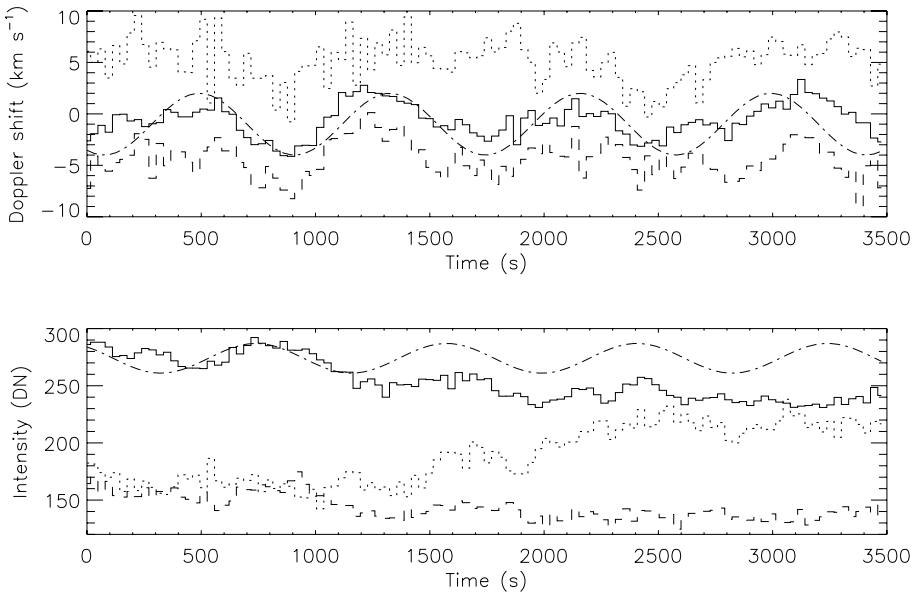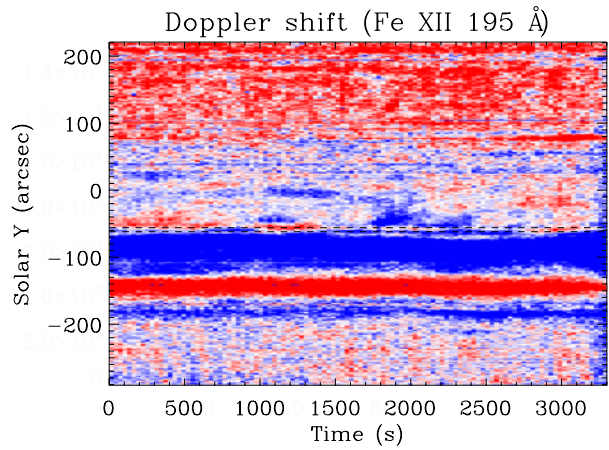cross in Fig. 12 (from Erdélyi
and Taroyan 2008)

Fig. 14 The Doppler shift and intensity time series averaged over five pixels between the dashed lines in Fig. 13. The *solid, dotted*, and *dashed curves* correspond to Fe XIX 195 Å, Fe X 184.7 Å, and Fe XIII 202 Å, respectively. The quarter-period phase shifted *dashed-dotted curves* represent sinusoidal fits to the Doppler shift and intensity oscillations (from Erdélyi and Taroyan 2008)

was applied to the intensity. A linear fit was subtracted from the time series to remove the background trend. A corresponding peak was found at 1.3 mHz with a 99% significance level. The slightly higher frequency could be due to the phase shifts as predicted by Taroyan and Bradshaw (2008).

The XRT and EIS images (Fig. 12) suggest that the oscillations correspond to a footpoint region of a loop where the slit crosses the loop. According to linear MHD wave theory, intensity and Doppler shift oscillations are usually associated with an acoustic longitudinal

wave. From the analysis of the XRT image, longitudinal motions at the marked location should have a line-of-sight component resulting in the observed Doppler shift. The XRT movie associated with the EIS observations shows that the oscillations are preceded by a small microflare near the footpoint, which would heat the plasma and trigger the oscillations similar to the events observed by SUMER in high-temperature lines (Wang et al. 2005). The microflare brightening starts at 20:30 UT and ends at 21:00 UT, i.e., around the time when the oscillation starts. The intensity increase seen in lower temperature lines (e.g., Fe VIII) and the decrease in higher temperature lines (e.g., Fe XII, Fe XIII, Ca XIII) conforms with the cooling scenario following a transient heat deposition. The rather slow damping is more obvious in the intensity than in the Doppler shift oscillations and requires further theoretical investigation. The quarter-period phase shift seen between the intensity and Doppler shift oscillations in Fig. 14 and their relative amplitudes also conform well with a standing-wave scenario (Taroyan and Bradshaw 2008).

Erdélyi and Taroyan (2008) presented a second example which is most likely a kink-type transverse oscillation. Density measurements were made using ratios between different Fe lines. Using these results a magnetic field strength of $B = 10 \pm 6$ G was derived. A similar example with magnetic field measurements has been presented by Van Doorsselaere et al. (2008).

8 Analysis of Doppler Shift Time Series as a New Diagnostic Tool

It must be mentioned that individual standing waves are not very often seen. An interesting and promising possibility for reliable inversion may come from the analysis of Doppler shift time series. The idea proposed by Taroyan et al. (2007b) is borrowed from helioseismology where the use of such time series has become a routine method for extremely precise diagnostics of the solar interior. The new method does not require the presence of coherent standing waves. The only underlying assumption is that the loops (or strands) are heated randomly both in time and in space in the longitudinal direction. No assumptions are made regarding the nature and the origin of the heating process.

The fundamentals of this novel idea can be elucidated using a simple analytical model. The model assumes that a 1D loop is in isothermal equilibrium. Small amplitude longitudinal motions inside the loop are governed by the following linear inhomogeneous equation:

$$\frac{\partial^2 v}{\partial t^2} - c_s^2 \frac{\partial^2 v}{\partial s^2} = -\frac{\gamma - 1}{\rho_0} \frac{\partial \mathcal{H}}{\partial s}, \quad 0 < s < L, \ 0 < t, \tag{5}$$

where L is the length of the loop, $v = v(s, t)$ is the longitudinal velocity and c_s, ρ_0 are the constant sound speed and density along the loop. The right-hand side of (5) represents the source term and the function $\mathcal{H} = \mathcal{H}(s, t)$ is the heating rate which needs to be specified. Equation (5) is supplied with the boundary conditions

$$v(0, t) = v(L, t) = 0, \quad 0 < t, \tag{6}$$

and the initial conditions

$$v(s, 0) = \frac{\partial v(s, 0)}{\partial t} = 0, \quad 0 < s < L. \tag{7}$$

The boundary conditions (6) are a mathematical manifestation of the effects of the dense chromosphere on small amplitude motions generated within the corona. The initial conditions (7) assume that the loop plasma is initially at rest. The problem (5)–(7) can be solved
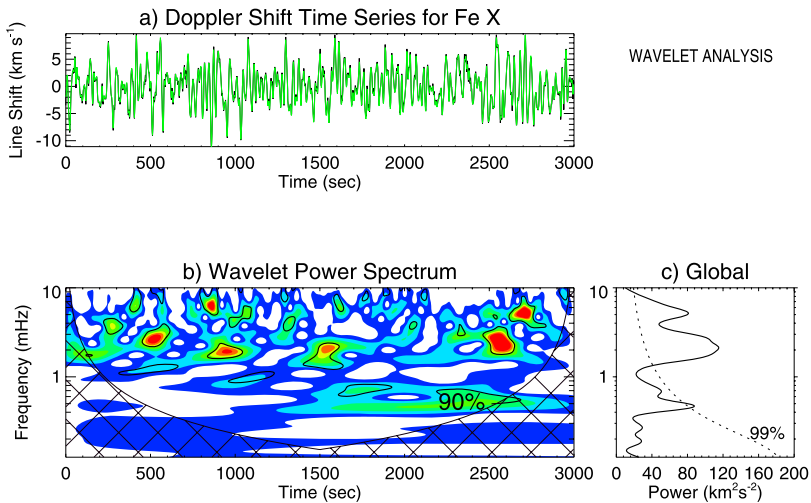
Fig. 15 (Color online) Wavelet analysis results corresponding to uniformly random heating along a 30 Mm long loop. The *top panel* (**a**) shows the Doppler shift time series in the Fe X line. The *bottom left panel* (**b**) displays the wavelet power spectrum. The *red color* represents high power and the *blue color* corresponds to low power. The *bottom right panel* (**c**) is the global wavelet spectrum. In the wavelet spectrum diagram (**b**), regions with 90% significance level are outlined in *black*. In the global wavelet diagram, the dotted lines indicate 99% significance level (from Taroyan et al. 2007b)

for different source terms representing random heating. The corresponding Green's function $G = G(s, t; \xi, \tau)$ is the solution to the equation

$$\frac{\partial^2 G}{\partial t^2} - c_s^2 \frac{\partial^2 G}{\partial s^2} = \delta(s - \xi)\delta(t - \tau), \quad 0 < s, \xi < L, \ 0 < t, \tau, \tag{8}$$

subject to the boundary conditions (6) and the initial conditions (7). Any solution to the inhomogeneous wave equation (5) can be expressed in terms of the Green's function, boundary conditions (6) and initial conditions (7). The results of the analytical study show that for a linear ideal 1D loop model heated by random pulses there is an infinite number of peaks in the velocity power spectrum corresponding to the frequencies of standing waves.

The inclusion of radiative losses, thermal conduction and nonlinearity introduces noise in the power spectrum. The most prominent peak corresponding to the fundamental mode is always present regardless of the random heating function and the heliographic position of the loop. This peak could therefore be used to determine the average temperature of the plasma inside the loop. The peak corresponding to the second harmonic only appears in the case of uniformly random heating. Peaks corresponding to the higher harmonics are not present due to their small amplitudes, losses and nonlinearity.

The results of the wavelet analysis for such a loop are displayed in Fig. 15. The Doppler shift time series measured in $\mathrm{km\,s^{-1}}$ is plotted in the top panel (a). The bottom left panel (b) displays the wavelet power spectrum. The right panel (c) represents the global wavelet spectrum (measured in $\mathrm{km^2\,s^{-2}}$) which is the sum of the wavelet power over time at each oscillation frequency. The red (blue) regions correspond to high (low) power. The crosshatched region indicates the cone of influence, where edge effects become important. In the wavelet spectrum diagram (b), regions with 90% significance level are outlined in black. In the global wavelet diagram, the dotted lines indicate 99% significance level. Loops heated
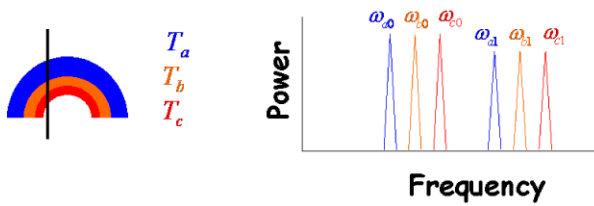
Multi-threaded loops

Fig. 16 *Left*: Cartoon representation of a multi-threaded loop. Each thread has its own temperature indicated by an index (a, b, c). The *black vertical line* represents a slit of a spectrometer crossing the loop. *Right*: The power spectrum contains multiple frequency peaks corresponding to different threads. The fundamental mode and the second harmonic for each thread are shown

near their footpoints only display the fundamental mode. This is mainly due to the large values of thermal conduction around the maximum of the second harmonic which results in strong damping. The phenomenon is explained in more detail by Taroyan et al. (2007b). The power spectrum analysis could therefore be used to establish the longitudinal distribution of the random heating. The power spectra are also sensitive to the temporal distribution of heating and, as a result, they could be used to estimate the average amount of energy involved in a single heating event. Interestingly, the peaks do not show up when the same analysis is applied to the intensity time series. This effect is explained by Taroyan and Bradshaw (2008).

Antolin et al. (2009) have recently applied the same technique in 1.5D. A loop is heated by the nonuniform conversion of Alfvén waves into slow and fast MHD shocks. Initial results show the presence of peaks in the power spectrum, similar to those obtained in the 1D study. The effect of nonlinearity is to broaden the peaks.

In principle, the power spectrum analysis could be applied in a more general situation, when both longitudinal (slow) and transverse (kink and Alfvénic) motions are taken into account. A possible problem could be the disentanglement of these motions during the loop evolution. However, a combination of spectroscopy with state of the art imaging observations in 3D (STEREO) could resolve this problem.

It has often been argued (see, for example, Parker 1988) that the loops consist of multiple threads. Understanding such multi-threaded structuring is a major issue in solar coronal physics. In this respect, the proposed method could be useful. Each thread would have a peak and possibly a corresponding overtone in the power spectrum as shown in Fig. 16. By studying these peaks, one could, in principle, determine the way in which the individual threads are heated and their average temperatures. However, this remains a speculation. Combined theoretical and observational work is needed in order to find out the extent of applicability of the proposed method.

9 Summary

Forward modeling and inversion are two complementary approaches which allow the heating problem to be tackled in an integrated and comprehensive manner. The new generation satellites have provided new constraints on theoretical models and triggered a wealth of studies which focus on the footprints and observable consequences of various theoretical

heating scenarios. These footprints often overlap with each other. Therefore future research is facing the task of disentangling the footprints in order to distinguish the predictions of various heating mechanisms.

Missions like Hinode, STEREO, SDO are most likely to provide further stringent constraints and trigger a new wave of studies in theoretical forward modeling. Being equipped with coordinated diagnostic capabilities, these missions are also expected to improve our understanding of the coronal plasma.

New inversion methods based on MHD waves are being developed. These methods have the potential to compete and serve as an alternative to more conventional inversion techniques. Standing longitudinal (acoustic type) waves in coronal loops are important for quantifying the unknown heating function. These waves are now detected both with SoHO/SUMER in high temperature lines and with Hinode/EIS in lower temperature lines.

The analysis of Doppler shift time series is a new efficient tool for determining the spatial and temporal distribution of the heating function. The method does not require the presence of individual coherent waves.

References

J. Andries, I. Arregui, M. Goossens, Astrophys. J. **624**, L57 (2005)

P. Antolin, K. Shibata, T. Kudoh et al., Astrophys. J. **688**, 669 (2008)

P. Antolin et al., Astrophys. J. (2009, in preparation)

T.D. Arber, A.W. Longbottom, C.L. Gerrard et al., J. Comp. Phys. **171**, 151 (2001)

M.J. Aschwanden, Astron. Astrophys. **560**, 1035 (2001)

M.J. Aschwanden, *Physics of the Solar Corona* (Springer, New York, 2006)

M.J. Aschwanden, C.E. Parnell, Astrophys. J. **572**, 1048 (2002)

M.J. Aschwanden, J. Terradas, Astrophys. J. **686**, L127 (2008)

M.J. Aschwanden, J.S. Newmark, J.-P. Delaboudiniere et al., Astrophys. J. **515**, 842 (1999)

M.J. Aschwanden, T.D. Tarbell, R.W. Nightingale, Astrophys. J. **535**, 1047 (2000)

M.J. Aschwanden, C.J. Schrijver, D. Alexander, Astrophys. J. **550**, 1036 (2001)

M.D. Aschwanden, A. Winebarger, D. Tsiklauri, H. Peter, Astrophys. J. **659**, 1673 (2007)

I. Ballai, R. Erdélyi, B. Pintér, Astrophys. J. **633**, L145 (2005)

D. Banerjee, R. Erdélyi, R. Oliver, E. O'Shea, Sol. Phys. **246**, 3 (2007)

A.O. Benz, S. Krucker, Astrophys. J. **568**, 413 (2002)

S.J. Bradshaw, R. Erdélyi, Astron. Astrophys. **483**, 301 (2008)

S.J. Bradshaw, H.E. Mason, Astron. Astrophys. **407**, 1127 (2003)

P. Brekke, D.M. Hassler, K. Wilhelm, Sol. Phys. **175**, 349 (1997)

P.K. Browning, Plasma Phys. Controlled Fusion **33**, 539 (1991)

E. Buchlin, P.J. Cargill, S.J. Bradshaw et al., Astron. Astrophys. **469**, 347 (2007)

P. Cargill, in *Solar System Plasma Physics: Resolution of Processes in Space and Time*, ed. by J.L. Birch, J.H. Waite Jr. (1993)

P.J. Cargill, Astrophys. J. **422**, 381 (1994)

P.J. Cargill, J.A. Klimchuk, Astrophys. J. **605**, 911 (2004)

B.K. Carter, R. Erdélyi, Astron. Astrophys. **475**, 323 (2007)

J. Chae, H.S. Yun, A.I. Poland, Astrophys. J. Suppl. **114**, 151 (1998)

N.B. Crosby, M.J. Aschwanden, B.R. Dennis, Sol. Phys. **143**, 275 (1993)

J.L. Culhane, L.K. Harra, A.M. James et al., Sol. Phys. **243**, 19 (2007)

I. De Moortel A, W. Hood, Astron. Astrophys. **408**, 755 (2003)

I. De Moortel, RSPTA **363**, 2743 (2005)

I. De Moortel, RSPTA **364**, 461 (2006)

I. De Moortel, S.J. Bradshaw, Sol. Phys. **252**, 101 (2008)

I. De Moortel, J. Ireland, R.W. Walsh, Astron. Astrophys. **355**, L23 (2000)

K.P. Dere, E. Landi, H.E. Mason, B.C. Monsignori, P.R. Young, Astron. Astrophys. Suppl. **125**, 149 (1997)

A.J. Díaz, R. Oliver, J.L. Ballester, Astrophys. J. **580**, 550 (2002)

J.G. Doyle, M.S. Madjarska, I. Roussev, L. Teriaca, J. Giannikakis, Astron. Astrophys. **396**, 255 (2002)

M.V. Dymova, M.S. Ruderman, Sol. Phys. **229**, 79 (2005)

R. Erdélyi, Astron. Geophys. **45**, 34 (2004)

R. Erdélyi, I. Ballai, Astron. Nacht. **328**, 726 (2007)

R. Erdélyi, B.K. Carter, Astron. Astrophys. **455**, 361 (2006)

R. Erdélyi, V. Fedun, Sol. Phys. **238**, 41 (2006)

R. Erdélyi, M. Goossens, Astron. Astrophys. **294**, 575 (1995)

R. Erdélyi, M. Goossens, Astron. Astrophys. **313**, 664 (1996)

R. Erdélyi, Y. Taroyan, Astron. Astrophys. **489**, L49 (2008)

R. Erdélyi, G. Verth, Astron. Astrophys. **462**, 743 (2007)

R. Erdélyi, M. Luna-Cardozo, C.A. Mendoza-Briceño, Sol. Phys. **252**, 305 (2008)

U. Feldman, Phys. Scr. **46**, 202 (1992)

L. Golub, J.M. Pasachoff, *The Solar Corona*. CUP (1997)

D.O. Gómez, Fund. Cosmic Phys. **14**, 131 (1990)

D. Gómez, P. Dmitruk, in *Proceedings of IAUS 247: Waves and Oscillations in the Solar Atmosphere: Heating and Magneto-Seismology*, ed. by R. Erdélyi, C.A. Mendoza-Briceño. IAUS, vol. 247, (2008)

M. Goossens, J. Andries, M.J. Aschwanden, Astron. Astrophys. **394**, L39 (2002)

B.V. Gudiksen, A. Nordlund, Astrophys. J. **618**, 1020 (2005a)

B.V. Gudiksen, A. Nordlund, Astrophys. J. **618**, 1031 (2005b)

V.H. Hansteen, Astrophys. J. **402**, 741 (1993)

M. Haynes, T.D. Arber, E. Verwichte, Astron. Astrophys. **479**, 235 (2008)

J.V. Hollweg, Astrophys. J. **254**, 806 (1982a)

J.V. Hollweg, Astrophys. J. **257**, 345 (1982b)

J.V. Hollweg, in *Mechanisms of Chromospheric and Coronal Heating*, ed. by P. Ulmschneider et al. (Springer, Berlin, 1991), p. 423

H.S. Hudson, Sol. Phys. **133**, 357 (1991)

J.A. Ionson, Astrophys. J. **226**, 650 (1978)

S.P. James, R. Erdélyi, Astron. Astrophys. **393**, L11 (2002)

D. Jess, M. Mathioudakis, R. Erdélyi, G. Verth, R.T.J. McAteer, F.P. Keenan, Astrophys. J. **680**, 1523 (2008)

R. Keppens, M. Nool, G. Tóth et al., Comput. Phys. Commun. **153**, 317 (2003)

B. Kliem, I.E. Dammasch, W. Curdt, K. Wilhelm, Astrophys. J. **568**, L61 (2002)

J.A. Klimchuk, Sol. Phys. **234**, 41 (2006)

J.A. Klimchuk, S.K. Antiochos, J.T. Mariska, Astrophys. J. **320**, 409 (1987)

T. Kosugi, K. Matsuzaki, T. Sakao et al., Sol. Phys. **243**, 3 (2007)

S. Krucker, A.O. Benz, Astrophys. J. **501**, L213 (1998)

T. Kudoh, K. Shibata, Astrophys. J. **514**, 493 (1999)

E. Landi, M. Landini, Astrophys. J. **618**, 1039 (2005)

E. Landi, G. Del Zanna, P.R. Young et al., Astrophys. J. Suppl. **162**, 261 (2006)

J.T. Mariska, Astrophys. J. **319**, 465 (1987)

J.T. Mariska, H.P. Warren, D.R. Williams et al., Astrophys. J. **681**, L41 (2008)

P. Mazzotta, G. Mazzitelli, S. Colafrancesco et al., Astron. Astrophys. Suppl. **133**, 403 (1998)

J.A. McLaughlin, L. Ofman, Astrophys. J. **682**, 1338 (2008)

C.A. Mendoza-Briceño, L.D.G Sigalotti, R. Erdélyi, Astrophys. J. **579**, L49 (2002)

C.A. Mendoza-Briceño, L.D.G Sigalotti, R. Erdélyi, Adv. Space. Phys. **32**, 995 (2003)

C.A. Mendoza-Briceño, L.D.G Sigalotti, R. Erdélyi, Astrophys. J. **605**, 493 (2004)

C.A. Mendoza-Briceño, L.D.G Sigalotti, R. Erdélyi, Astrophys. J. **624**, 1080 (2005)

S. Moriyasu, T. Kudoh, T. Yokoyama, K. Shibata, Astrophys. J. **601**, L107 (2004)

V.M. Nakariakov, L. Ofman, Astron. Astrophys. **372**, L53 (2001)

V.M. Nakariakov, E. Verwichte, LRSP **2**, 3 (2005)

V.M. Nakariakov, D. Tsiklauri, A. Kelly et al., Astron. Astrophys. **414**, L25 (2004)

U. Narain, P. Ulmschneider, Space Sci. Rev. **75**, 453 (1996)

L. Ofman, J.M. Davila, Astrophys. J. **456**, L123 (1996)

L. Ofman, T.J. Wang, Astrophys. J. **580**, L85 (2002)

E. O'Shea, A.K. Srivastava, J.G. Doyle, D. Banerjee, Astron. Astrophys. **473**, L13 (2007)

E.N. Parker, Astrophys. J. **330**, 380 (1988)

C.E. Parnell, P.E. Jupp, Astrophys. J. **529**, 554 (2000)

S. Patsourakos, J.A. Klimchuk, Astrophys. J. **628**, 1023 (2005)

H. Peter, P.G. Judge, Astrophys. J. **522**, 1148 (1999)

H. Peter, B. Gudiksen, A. Nordlund, Astrophys. J. **617**, L85 (2004)

S. Poedts, M. Goossens, W. Kerner, Astrophys. J. **360**, 279 (1990)

E. Priest, T. Forbes, *Magnetic Reconnection* (Cambridge University Press, Cambridge, 2000). ISBN 0521481791

E.R. Priest, C.R. Foley, J. Heyvaerts, T.D. Arber, J.L. Culhane, L.W. Acton, Nature **393**, 545 (1998)

F. Reale, Astrophys. J. **580**, 566 (2002)

F. Reale, A. Ciaravella, Astron. Astrophys. **449**, 1177 (2006)

B. Roberts, V.M. Nakariakov, in *Turbulence, Waves and Instabilities in the Solar Plasma*, ed. by R. Erdélyi et al. NATO Science Ser., vol. 124 (2003), p. 167

M.S. Ruderman, R. Erdélyi, in *Waves, Oscillations and Small-Scale Transient Events in the Solar Atmosphere: A Joint View from SOHO and TRACE*, ed. by R. Erdélyi, J.L. Ballester, B. Fleck. ESA-SP vol. 547 (2004), p. 507

M.S. Ruderman, B. Roberts, Astrophys. J. **577**, 475 (2002)

G.D. Sandlin, G.E. Brueckner, R. Tousey, Astrophys. J. **214**, 898 (1977)

L.M. Sarro, R. Erdélyi, J.G. Doyle, M.E. Pérez, Astron. Astrophys. **351**, 721 (1999)

J.T. Schmelz, P.C.H. Martens, Astrophys. J. **636**, L49 (2006)

M. Selwa, K. Murawski S, K. Solanki, Astron. Astrophys. **436**, 701 (2005)

M. Selwa, L. Ofman, K. Murawski, Astrophys. J. **668**, L83 (2007)

T. Shimizu, Publ. Astron. Soc. Jpn. **47**, 251 (1995)

L.D.G. Sigalotti, C.A. Mendoza-Briceño, M. Luna-Cardozo, Sol. Phys. **246**, 187 (2007)

D. Spadaro, G. Noci, R. Zappalà, S.K. Antiochos, Astrophys. J. **355**, 342 (1990)

Y. Taroyan, S.J. Bradshaw, Astron. Astrophys. **481**, 247 (2008)

Y. Taroyan, R. Erdélyi, J.G. Doyle, S.J. Bradshaw, Astron. Astrophys. **438**, 713 (2005)

Y. Taroyan, S.J. Bradshaw, J.G. Doyle, Astron. Astrophys. **446**, 315 (2006)

Y. Taroyan, R. Erdélyi, T.J. Wang, S.J. Bradshaw, Astrophys. J. **659**, L173 (2007a)

Y. Taroyan, R. Erdélyi, J.G. Doyle, S.J. Bradshaw, Astron. Astrophys. **462**, 331 (2007b)

L. Teriaca, D. Banerjee, J.G. Doyle, Astron. Astrophys. **349**, 636 (1999a)

L. Teriaca, J.G. Doyle, R. Erdélyi, L.M. Sarro, Astron. Astrophys. **352**, L99 (1999b)

C. Torrence, G.P. Compo, Bull. Am. Meteor. Soc. **79**, 61 (1998)

I. Ugarte-Urra, J.G. Doyle, R.W. Walsh, M.S. Madjarska, Astron. Astrophys. **439**, 351 (2005)

P. Ulmschneider, in Lect. Notes in Phys., vol. 507, ed. by J.-C. Vial et al. (1998), p. 77

A.A. van Ballegooijen, Astrophys. J. **311**, 1001 (1986)

T. Van Doorsselaere, J. Andries, S. Poedts, Astron. Astrophys. **471**, 311 (2007)

T. Van Doorsselaere, V.M. Nakariakov, P.R. Young, E. Verwichte, Astron. Astrophys. **487**, L17 (2008)

G. Verth, T. van Doorsselaere, R. Erdélyi, M. Goossens, Astron. Astrophys. **475**, 341 (2007)

G. Verth, R. Erdélyi, D.B. Jess, Astrophys. J. **678**, L45 (2008)

E. Verwichte, M. Haynes, T.D. Arber et al., Astrophys. J. **685**, 1286 (2008)

R.W. Walsh, J. Ireland, Astron. Astrophys. Rev. **12**, 1 (2003)

R.W. Walsh, G.E. Bell, A.W. Hood, Sol. Phys. **171**, 81 (1997)

T.J. Wang, S.K. Solanki, W. Curdt et al., Astrophys. J. **574**, L101 (2002)

T.J. Wang, S.K. Solanki, W. Curdt et al., Astron. Astrophys. **406**, 1105 (2003a)

T.J. Wang, S.K. Solanki, D.E. Innes et al., Astron. Astrophys. **402**, L17 (2003b)

T.J. Wang, S.K. Solanki, D.E. Innes et al., Astron. Astrophys. **435**, 753 (2005)

T.J. Wang, D.E. Innes, S.K. Solanki, Astron. Astrophys. **455**, 1105 (2006)

T.J. Wang, D.E. Innes, J. Qiu, Astrophys. J. **656**, 598 (2007)

A.R. Winebarger, H.P. Warren, J.T. Mariska, Astrophys. J. **587**, 439 (2003)

T.V. Zaqarashvili, Astron. Astrophys. **399**, L15 (2003)

J.B. Zirker, Sol. Phys. **148**, 43 (1993)